The hydrodynamic response of the sediment-water interface to coherent turbulent motions

Joey J. Voermans[1,2], **Marco Ghisalberti**[1,2], **and Gregory N. Ivey**[1,3]

[1]Ocean Graduate School, University of Western Australia, Perth, Australia.
[2]Department of Infrastructure Engineering, University of Melbourne, Melbourne, Australia.
[3]The UWA Oceans Institute, University of Western Australia, Perth, Australia.

Key Points:

- Sweep events can penetrate across the sediment-water interface and induce periods of significant flow variability across the interface.
- Coherent turbulent motions cause instantaneous momentum fluxes to greatly exceed the mean bed shear stress.
- By penetrating into the sediment bed, coherent turbulent motions increase the effective roughness experienced by the overlying flow.

Corresponding author: J.J. Voermans, jvoermans@unimelb.edu.au

Abstract

Unique observations of the hydrodynamics across the sediment-water interface (SWI) are used to quantify the instantaneous response of the interstitial fluid to the passage of coherent turbulent motions in the overlying flow. Over a range of permeability Reynolds numbers $Re_K = \sqrt{K}u_*/\nu$ (where K is the sediment permeability, u_* is the shear velocity and ν is the fluid viscosity), the passage of these turbulent motions create velocity fluctuations and momentum fluxes at the SWI to greatly exceed their mean values. Sweep motions are observed to penetrate into the sediment bed and induce instantaneous momentum fluxes that can be an order of magnitude larger than the mean bed shear stress. By penetrating into the sediment bed, the turbulent motions increase the effective roughness experienced by the flow and therefore the flow resistance. The properties of the mean flow alone are thus insufficient to describe the interaction of the overlying flow with the sediments.

1 Introduction

In bottom boundary layer flows, coherent turbulent motions (i.e. a fluid region where turbulence properties exhibit significant correlation in time and/or space [e.g. *Robinson*, 1991]) dominate the transport of mass, energy and momentum in the overlying flow and consist of sequences of sweeps, where high momentum fluid moves towards the bed, and ejections, where low momentum fluid moves away from the bed [e.g. *Roy et al.*, 2004; *Detert et al.*, 2010; *Adrian and Marusic*, 2012]. Though the presence of the sediment bed strongly diminishes the impact of these turbulent motions on the interface (i.e. due to viscous damping effects), there is some evidence to suggest that these turbulent motions can penetrate below the sediment-water interface (SWI) [*Nelson et al.*, 1995; *O'Connor and Hondzo*, 2008]. When coherent turbulent motions modulate the flow at the SWI, they are likely to play a critical role in physical and biochemical processes operating across the interface, including particle entrainment, boundary resistance to the flow, contaminant release from the sediment bed and organic matter cycling [*Grant and Marusic*, 2011; *Manes et al.*, 2012; *Schmeeckle*, 2014; *Grant et al.*, 2018].

The extent to which the turbulent motions in the overlying flow can impact the hydrodynamics at the SWI is strongly dependent on both the intensity of the flow and the characteristics of the sediment bed. The permeability Reynolds number $Re_K = \sqrt{K}u_*/\nu$ (where K is the permeability of the sediment bed, u_* is the shear velocity and a measure of the bed shear stress and ν is the fluid viscosity) is thus expected to be the key parameter as it defines whether turbulent effects are able to pass across the SWI [*Voermans et al.*, 2018]. When $Re_K \leq O(0.01)$ (when the permeability is low or the flow is weak) the sediment bed behaves as an impermeable boundary, while for $Re_K \geq O(1)$ (when the permeability or flow strength is high) turbulence begins to dominate the transport of mass and momentum across the SWI [*Voermans et al.*, 2017, 2018]. As typical aquatic sediments are found within the range of $Re_K = O(0.001 - 10)$ [e.g. *Wilson et al.*, 2008; *Voermans et al.*, 2017], the interfacial hydrodynamics of many aquatic sediments are thus likely impacted by the passage of coherent turbulent motions in the overlying flow.

The impact of coherent turbulent motions on the SWI region remains, however, uncertain due to the technical difficulties in measuring the flow close to the sediment bed, let alone at the interface itself. In this experimental study, a combination of refractive index matching (RIM) and particle tracking velocimetry (PTV) enabled measurements of the mean flow and turbulence simultaneously above and within a stationary sediment bed. This enables direct observations of the hydrodynamic response at and below the interface to the passage of coherent turbulent motions in the overlying flow. Using conditional sampling of the most energetic turbulent motion in the overlying flow, we examine the connection between these coherent motions and the instantaneous momentum fluxes, streamwise and vertical velocity fluctuations at and across the interface.

2 Methodology

Experiments were carried out in a 2-m-long and 0.4-m-wide flume at the University of Western Australia. Instantaneous flow fields across the SWI were obtained by combining RIM with PTV (for more details see *Voermans et al.* [2017]). The working fluid was a 59% sodium iodide by mass solution (with a fluid density $\rho = 1770$ kg/m^3 and $\nu = 1.35 \times 10^{-6}$ m^2/s), which had a refractive index of $n = 1.4750$ and was equal to that of the borosilicate glass spheres used as model for sediments. Three different diameters were used for the flat, stable and monodisperse granular bed, namely $d = 6$, 10 and 25 mm, with corresponding permeability $K = 0.04$, 0.11 and 0.69 mm^2, respectively, and were estimated using the Carman−Kozeny model. The flow was seeded with silver coated PMMA particles (with a diameter of 32-40 µm for $d = 6$ and 10 mm, and 91-100 µm for $d = 25$ mm), and were continuously illuminated by a laser sheet (with a width of either 1 mm for $d = 6$ and 10 mm, or 3 mm for $d = 25$ mm). Due to the refractive index matching, the reflected light of the tracer particles was undistorted by the presence of the sediment bed and the local positions of the particles were accurately captured by a camera imaging the light sheet both above and below the SWI. The frames were recorded at a rate of 23 frames per second, covering a region of 35×70 mm (for $d = 6$ and 10 mm) or 90×180 mm (for $d = 25$ mm). The captured images were post-processed in the PTV-software Streams [*Nokes*, 2016] to obtain 2D-velocity fields, where u and w are the velocity components in the longitudinal (x) and wall-normal directions (z), respectively. In this study, the SWI at $z = 0$ is defined as the vertical position of the inflection point in the vertical porosity profile θ.

The measured flow properties (ξ) were decomposed in time $\xi = \overline{\xi} + \xi'$ and in space $\overline{\xi} = \langle\overline{\xi}\rangle + \tilde{\xi}$, where the overbar indicates time-averaging and brackets indicate spatial averaging over the fluid domain; ξ' and $\tilde{\xi}$ are the temporal and spatial varying components of ξ, respectively (for more details see *Nikora et al.* [2007]). The double-averaged fluid shear stress τ is then given by $\tau(z) = \rho\nu\partial(\theta\langle\overline{u}\rangle)/\partial z - \rho\theta\langle\overline{u'w'}\rangle - \rho\theta\langle\tilde{u}\tilde{w}\rangle$ [*Nikora et al.*, 2001]. In this study, the shear velocity is defined as $u_* = \sqrt{\tau_{max}/\rho}$ (as in *Voermans et al.* [2017]), where τ_{max} is the maximum fluid shear stress observed at the vertical position $z = z_*$. The flow velocities of the experiments were in the range $U_\delta = 31 - 160$ mm/s (measured at the top of the turbulent boundary layer $z = \delta$), giving Re_K of 0.47 – 6.3, $Re_* = \delta u_*/\nu$ of 82 – 536 and $Re_\delta = \delta U_\delta/\nu$ of 1192 – 7567. The Reynolds numbers (i.e., Re_* and Re_δ) of the flows studied are small compared to the those typically observed in aquatic systems. However, as coherent turbulent motions dominate the hydrodynamics near the sediment bed in both high and low Reynolds number flows [e.g. *Kim et al.*, 1987; *Adrian and Marusic*, 2012], the small Reynolds numbers in this study are not considered to be a limitation in assessing the hydrodynamic response of the interface to the passage of coherent turbulent motions in the overlying flow. Nevertheless, the smallest Re_K-case as originally presented in *Voermans et al.* [2017] is not included in this study.

2.1 Conditional sampling procedure

The dominant turbulent structures in the overlying flow are identified by means of quadrant analysis, where the Reynolds stress ($u'w'$) is decomposed into four quadrants (outward interactions $u' > 0$, $w' > 0$; ejections $u' < 0$, $w' > 0$; inward interactions $u' < 0$, $w' < 0$ and sweeps $u' > 0$, $w' < 0$). The Reynolds stress component was first smoothed by a moving averaging window with a length of $t^+ \approx 15$ (where the superscript '+' denotes normalization with the viscous timescale ν/u_*^2) to remove spikes. The time scale of the moving averaging window is similar to that used by *Blackwelder and Kaplan* [1976]. A smoothed variable is indicated by a subscript '*m*'. Large sweep and ejection events were identified by the criterion:

$$\begin{gathered}(u'w')_m < -H|\overline{u'w'}| \\ \text{and } (u'w')_m \text{ is a local minimum}\end{gathered} \tag{1}$$

where $H = 2$ is a threshold value, as in *Subramanian et al.* [1982]. As the large turbulent motions observed near the sediment bed are three-dimensional coherent structures and can vary in shape and size, conditional averaging over either the identified ejection or sweep events can give a distorted image of the actual turbulent structure (e.g. *Subramanian et al.* [1982]). Therefore, the foregoing identification method is extended to identify the shear layer that separates the high and low momentum region (sweep and ejection, respectively) and can be seen as the 'central feature' of the large turbulent motion. The center is identified by the positive zero-crossing of the turbulent streamwise component which identifies the local transition from an ejection to a sweep event:

$$(u'_m) = 0 \quad \text{and} \quad \frac{d(u'_m)}{dt} > 0 \tag{2}$$

For every sweep event, the centre is identified by the first positive zero-crossing of $(u')_m$ prior to the sweep event, while for every ejection event the centre is identified after the ejection event (see Figure S1). Conditional averaging is then performed over the identified centers of both the sweep and ejection events, where the conditional average of an instantaneous quantity ξ is determined by:

$$\xi_c(\Delta t) = \frac{1}{n}\sum_{i=1}^{n}\xi(t_d + \Delta t) \tag{3}$$

where ξ_c is the conditionally-averaged quantity of property ξ, t_d are the detected instants of events, Δt is the time relative to t_d, and n is the total number of identified events [e.g. *Antonia et al.*, 1990]. Note that the conditional averaging is performed over the non-smoothed instantaneous quantities. The conditional averaging technique based on the Reynolds stress component (1) is favoured over other techniques as it ensures that the largest sweep and ejection events are included in the conditioning analysis (e.g. *Bogard and Tiederman* [1986]).

3 Results and Discussion

The impact of turbulent motions in the overlying flow on the instantaneous flow properties across the permeable SWI is illustrated by the pre-multiplied energy spectra of the streamwise velocity fluctuations $f\phi_{uu}/u_*^2$ (where $f = 1/T$ is the frequency, T is the period and ϕ_{uu} is the spectral density of the streamwise velocity fluctuations). Energetic turbulent scales are observed above the interface, focused around the spectral-peak vertically positioned at z_s^+ and with a period T_s^+ (see Figure 1 for two example cases, $Re_K = 0.78$ and $Re_K = 3.9$). The properties of the spectra peak vary across the range of experiments, with the range of vertical positions being $z_s^+ = 14 - 105$ and periods of $T_s^+ = 26 - 142$ (Table S1). The time scale T_s that corresponds to the range of most energetic turbulence time scales observed at and below the SWI, and demonstrates that the large turbulent motions in the overlying flow control the turbulent hydrodynamic features across the SWI and into the interstitial fluid. The depth of flow penetration below the SWI is observed to increase with increasing Re_K [*Voermans et al.*, 2017].

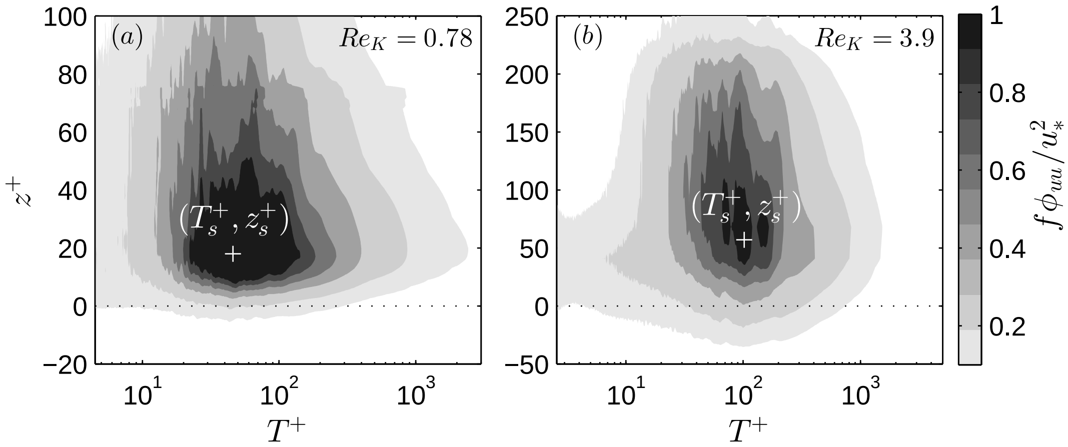

Figure 1. Pre-multiplied energy spectrum of the streamwise velocity fluctuations ($f\phi_{uu}/u_*^2$) for (a) $Re_K = 0.78$ and (b) $Re_K = 3.9$. Period (T^+) and vertical position (z^+) are normalized by viscous scales. The spectral-peak is located at the vertical position z_s^+ where the time scale T_s^+ is the time scale of the most energetic turbulent motion.

To identify the response of the interfacial hydrodynamics to the passage of these energetic turbulent motions in the overlying flow (characterized by the time scale T_s), the conditional sampling procedure is performed at the vertical position $z = z_s$. Two examples of the two-dimensional spatial structure of the conditionally-averaged turbulence velocity field are shown in Figure 2 (for $Re_K = 0.78$ and $Re_K = 3.9$), where the position at which the central features of the turbulent motions are identified is marked by a black dot. The turbulent motion corresponds to a high momentum region overlapping a low momentum region and is consistent with that of a large sweep and ejection event, respectively. For $Re_K = 0.78$, the observed shear layer separating these regions is inclined at an angle of approximately 20°, comparable to those typically observed in the turbulent boundary layer [e.g. *Adrian et al.*, 2000; *Detert et al.*, 2010]. For $Re_K = 3.9$ the inclination angle is observed to be much higher at about 40°, although such larger angles are not completely uncommon and have, for instance, been seen in flows over gravel beds [*Buffin-Bélanger et al.*, 2000].

Conditionally-averaged vertical profiles of the streamwise velocity and the turbulent momentum flux at two different longitudinal positions are shown in Figure 3 (a small and sheltered pore in red and a larger pore in gray-scale for the case of $Re_K = 3.9$). The spatial heterogeneity of the SWI impacts a thin region across the SWI (i.e. $O(d)$), where the

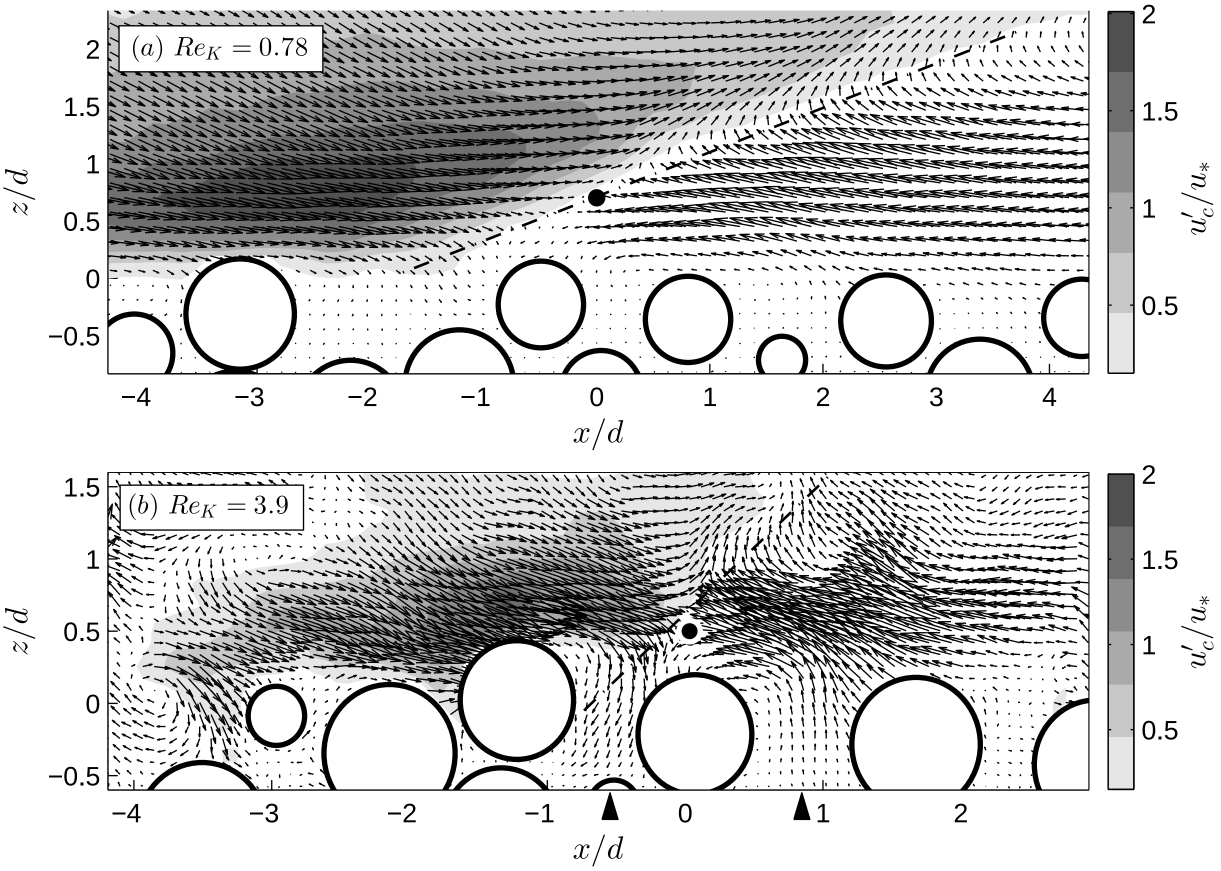

Figure 2. Conditionally-averaged turbulence velocity fields for (a) $Re_K = 0.78$ and (b) $Re_K = 3.9$, based on the conditional sampling performed at the position identified by the black circle. The mean flow is from left to right and gray patches correspond to the magnitude of the high momentum region ($u'_c/u_* > 0$). Profiles of the streamwise velocity and the turbulent momentum flux during the sweep and ejection event at $x/d = -0.55$ and $x/d = 0.85$ in (b) are given in Figure 3.

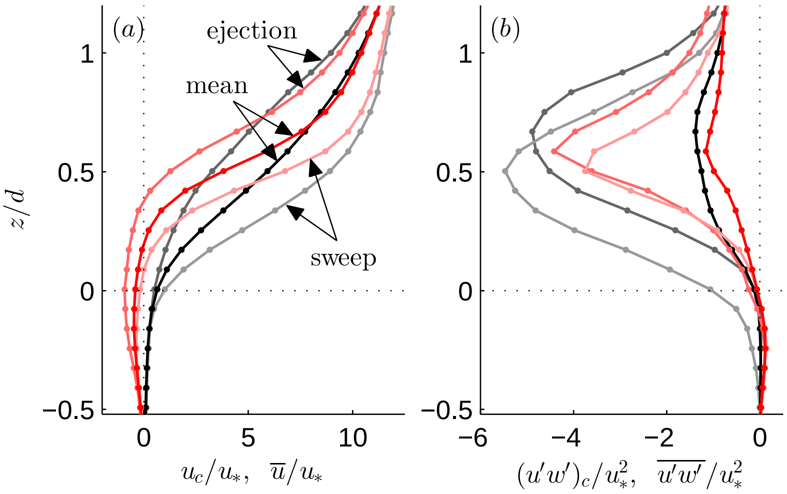

Figure 3. Conditionally-averaged vertical profiles of (a) the streamwise velocity (u_c/u_*) and (b) the turbulent momentum flux ($(u'w')_c/u_*^2$) during sweep and ejection events at the horizontal positions $x/d = 0.55$ (red-scale) and $x/d = 0.85$ (grey-scale) for $Re_K = 3.9$ as shown in Figure 2b. Time averaged profiles at these positions are given in red and black. The horizontal dashed lines correspond to the position of the SWI.

streamwise velocity is consistently enhanced during the sweep event and consistently reduced during the ejection event (Figure 3a). While the impact of the ejection and sweep events on the hydrodynamics at $z = 0$ can be weak for some pores (e.g. see the red curves in Figure 3b), the instantaneous sweep events are responsible for momentum fluxes across the SWI that are a factor of 8 larger than the time averaged turbulent momentum fluxes (e.g. see the light grey curve in Figure 3b).

The temporal variability of the hydrodynamics at z_s is obtained by spatially averaging the conditionally-averaged time series of the flow properties at each point in the horizontal plane positioned at z_s. The resulting time series of the streamwise and vertical velocity fluctuations at z_s (Figure 4a,c) are consistent with the spatial structure of the turbulent motion observed in Figure 2, corresponding to a low momentum fluid region with upward flow ($t < 0$) and high momentum fluid region with downward flow ($t > 0$). As the normalized instantaneous streamwise velocity remains nearly independent of Re_K, it suggests that the large turbulent motion in the overlying flow remains structurally similar irrespective of the sediment permeability. The observed increase of the relative vertical velocity fluctuations with Re_K is consistent with the weakening of the wall-blocking effect [e.g. *Perot et al.*, 1995; *Voermans et al.*, 2017]. The time series of the instantaneous tur-

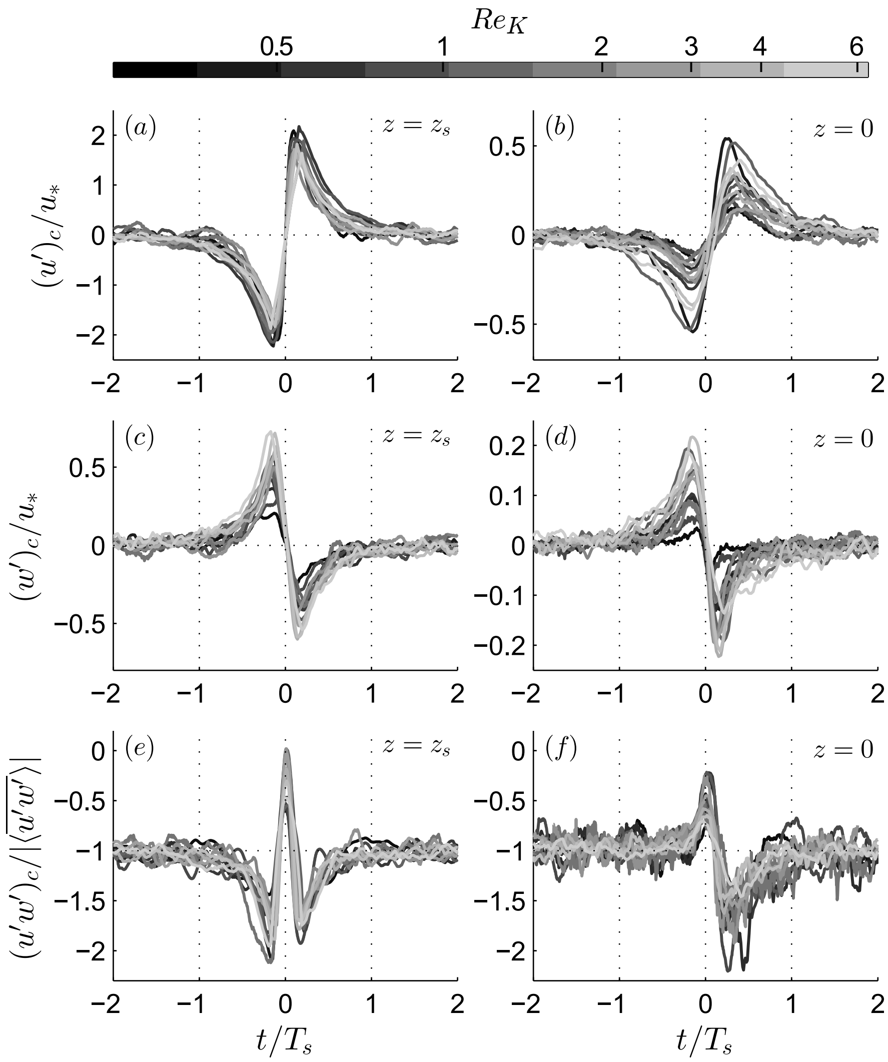

Figure 4. Conditionally-averaged time series of the streamwise velocity fluctuations, vertical velocity fluctuations and turbulent momentum fluxes above the SWI (a, c and e, respectively) and at the SWI (b, d and f), for all experimental cases (Re_K = 0.47 to Re_K = 6.3 is from black to light grey, respectively).

bulent momentum flux at z_s demonstrates the correlation between the regions of low and high momentum to ejection and sweep events, respectively. Note that the time scale associated with the temporal coherence of the flow properties in Figures 4a,c,e is comparable to the spectral peak period T_s, which suggests that the conditional averaging technique indeed captures the most energetic turbulent motion in the overlying flow.

The turbulent structures identified at z_s can be used to determine the interfacial response to the passage of these large turbulent motions. The time series of the streamwise and vertical velocity fluctuations at the SWI (Figure 4b,d) correlate strongly to the passage of the ejection event (decreasing streamwise velocity and upward flow) and the sweep event (enhanced streamwise velocity and downward flow). No apparent trend can, however, be observed between the magnitude of the streamwise velocity fluctuations and either Re_K or Re_*. The intensity of the vertical velocity fluctuations at the SWI increases with increasing Re_K. While the sweep events are able to penetrate to the SWI (Figure 4f), ejection events do not reach the interface as the instantaneous turbulent momentum flux returns to the background Reynolds stress for $t < 0$. As the enhanced interfacial flow properties during the passage of the sweep event are sustained over durations comparable to the period of most energetic turbulent motion in the flow, this suggests that sweep events originating in the overlying flow dominate the temporal variability of the interfacial hydrodynamics.

As both the instantaneous streamwise velocity and the turbulent momentum flux are largest during the passage of the sweep events, it is expected that these turbulent motions in the overlying flow cause significant variability of the total fluid stresses on the sediment bed, and hence the climatology of the SWI. The temporal and spatial variability of the total fluid stress on the sediments is estimated by the sum of the instantaneous viscous and turbulent momentum flux contributions. Consistent with our definition of the shear velocity u_*, the instantaneous momentum flux M is then taken at the vertical position $z = z_*$ (i.e. the height above the bed at which the spatially averaged fluid shear stress is maximum), and is typically positioned below z_s where $z_*/z_s \approx 0.85 \pm 0.25$. M is then given by:

$$M(z_*, t) \approx \rho\nu \frac{\partial(\theta u)}{\partial z} - \rho\theta u' w' \qquad (4)$$

In Figure 5a, the probability density functions (PDFs) of the normalized instantaneous momentum flux M/τ_b (where $\tau_b = \rho u_*^2$ is the bed shear stress) for all experimental cases are

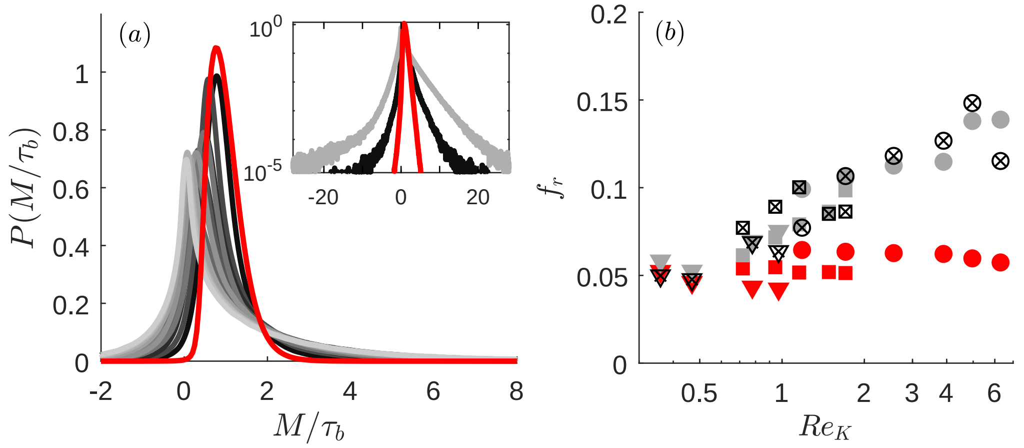

Figure 5. (a) Probability density functions (PDFs) of the normalized instantaneous momentum flux towards the sediment bed M/τ_b for all experimental cases (Re_K = 0.47 to Re_K = 6.3 is from black to light grey respectively; Re_K = 0 is given in red [DNS results from *Örlü and Schlatter*, 2011]; semi-logarithmic scaling in insert, for Re_K = 0.47 and Re_K = 6.3 only). (b) Comparison of the measured friction factor f_r for our experiments (white with crosses) against those predicted based on an effective wall roughness k_s with and without consideration of the turbulent shear stress penetration depth δ_p (grey and red, respectively): (inverted triangle) d = 6 mm, (square) d = 10 mm and (circle) d = 25 mm.

compared against observations of the bed shear stress at an impermeable smooth boundary (in red, from *Örlü and Schlatter* [2011]). Note that for impermeable and smooth boundaries, the instantaneous momentum flux at z_* is, by definition, equal to the instantaneous bed shear stress. For decreasing Re_K, the PDF of the instantaneous momentum flux tends to return to that observed at impermeable boundaries and is consistent with the concept of impermeable boundary behaviour for $Re_K \ll 1$ [*Voermans et al.*, 2017]. Conversely for increasing Re_K, strong deviations are observed at the tails of the PDFs with more frequent peak events and a large increase in peak magnitude (Figure 5a), where peak values are $M/\tau_b = O(1)$ for an impermeable boundary whereas $M/\tau_b = O(10)$ for $Re_K = O(1)$ (see also the variability of extreme momentum flux events with Re_K in Figure S2). As 95% of the large bed shear stress events (of $M/\tau_b > 5$) are identified by the conditional averaging technique and therefore included in the time-series shown in Figure 4, it is likely that the most energetic turbulent motions (as identified in Figures 2 and 4) are responsible for the long tails observed in the PDFs of the instantaneous momentum flux towards the sediment bed (Figure 5a). The coherent turbulent structures in the overlying flow thus have the ability to significantly alter the instantaneous hydrodynamics across the SWI.

Our experimental observations suggest that the large turbulent motions are able to penetrate deeper into the sediment bed with increasing Re_K, consistent with the observed increase of the turbulent shear stress penetration depth δ_p [*Voermans et al.*, 2017, 2018]. Note, δ_p can be estimated by $(\delta_p u_*)/\upsilon \simeq 8Re_K^{1.8}$ [*Voermans et al.*, 2018]. While this has major implications for many interfacial processes sensitive to the instantaneous variations of the flow (e.g., the initiation of sediment motion [*Coleman and Nikora*, 2008; *Diplas et al.*, 2008]), and the depth to which rapid mixing can occur (e.g., solute transport and contaminant release), the flow resistance of the bed is also strongly impacted by the quasi-periodic penetration of the large turbulent motions into the sediments. *Manes et al.* [2011, 2012] argued that the penetration of turbulence into the sediment bed increases the roughness height k_s and thus the flow resistance of the sediment bed.

Flow resistance is typically characterized by a friction factor, defined here as $f_r = 8(u_*^2/U_b^2)^{1/2}$, and relates the energy loss by friction to the depth-averaged velocity $U_b = [1/(\delta+\delta_p)]\int_{-\delta_p}^{\delta}\theta\langle\overline{u}\rangle dz$. By integrating the logarithmic law of the wall, the friction factor f_r can be determined through $(8/f_r)^{1/2} = (1/\kappa)\ln(11\delta/k_s)$ [e.g. *Ferguson*, 2007], with $\kappa \approx 0.4$. The roughness height is initially taken here as the distance between the SWI and the top of the sediment bed, giving $k_s \approx 0.3d$ [*Voermans et al.*, 2017]. Values of f_r predicted with this roughness height are found to be equal to our measured values for small Re_K, but increasingly underestimate f_r when Re_K increases (Figure 5b). However, by redefining k_s as the distance from the top of the sediment bed down to the depth to which the turbulent motions penetrate into the sediment bed, i.e. $k_s = 0.3d + \delta_p$, excellent agreement is obtained between the measured and predicted friction factors (Figure 5b). Hence, the following model for the prediction of flow resistance is proposed:

$$\sqrt{\frac{8}{f_r}} = \frac{1}{\kappa}\ln\left(\frac{11\delta}{0.3d + \frac{8Re_K^{1.8}\upsilon}{u_*}}\right) \qquad (5)$$

By penetrating into the sediment bed, the turbulent motions increase the effective roughness experienced by the flow and thus increases the flow resistance. This not only demonstrates the critical role of the large turbulent motions in the description of the interfacial hydrodynamics, but also implies that the mean flow properties alone are insufficient to describe the interaction between the flow and sediments in aquatic systems.

4 Conclusions

Experimental observations of flow fields across the SWI show that turbulent motions in the overlying flow above the sediment bed induce strong variability in hydrodynamic properties across the SWI. The dominant turbulent motions in the flow consist of sequences of events where high momentum fluid moves towards the sediment bed (sweep) and low speed fluid moves away from the sediments (ejection). Conditionally-averaged time series demonstrate that sweep events cause episodes of enhanced instantaneous velocity and turbulent momentum fluxes at the interface. The simultaneous occurrence of increases in streamwise velocity and turbulent momentum fluxes during the passage of the sweep event causes peak stress events on the sediment bed, and these events become more intense with increasing Re_K. For typical aquatic sediments, this creates instantaneous momentum fluxes towards the sediment bed that can be up to one order of magnitude larger than the peak bed shear stress events observed at an impermeable and smooth boundary. By penetrating into the sediment bed, these turbulent motions increase the resistance of the sediments to the flow. Hence, the large turbulent motions in the overlying flow play a critical role in the dynamic interaction between the overlying flow and the sediment bed.

Acknowledgments

This research was supported under the Australian Research Council's Discovery Projects funding scheme (project no. DP120102500). The authors would like to thank the reviewers for their comments and suggestions. The data used in creating the figures is available in a repository (doi:10.5281/zenodo.1217818).

References

Adrian, R. J. and Marusic, I. (2012). Coherent structures in flow over hydraulic engineering surfaces. *Journal Hydraul. Res.* 50(5), 451–464.

Adrian, R. J., Meinhart, C. D. and Tomkins, C. D. (2000). Vortex organization in the outer region of the turbulent boundary layer. *J. Fluid Mech.* 422, 1–54.

Antonia, R. A., Bisset, D. K. and Browne, L. W. B. (1990). Effect of Reynolds number on the topology of the organized motion in a turbulent boundary layer. *J. Fluid Mech.* 213, 267–286.

Blackwelder, R. F. and Kaplan, R. E. (1976). On the wall structure of the turbulent boundary layer. *J. Fluid Mech.* 76(1), 89–112.

Bogard, D. G. and Tiederman, W. G. (1986). Burst detection with single-point velocity measurements. *J. Fluid Mech.* 162, 389–413.

Buffin-Bélanger, T., Roy, A. G. and Kirkbride, A. D. (2000). On large-scale flow structures in a gravel-bed river. *Geomorphology* 32(3), 417–435.

Coleman, S. E. and Nikora, V. I. (2008). A unifying framework for particle entrainment. *Water Resour. Res.* 44(4), W04415.

Detert, M., Nikora, V. and Jirka, G. H. (2010). Synoptic velocity and pressure fields at the water–sediment interface of streambeds. *J. Fluid Mech.* 660, 55–86.

Diplas, P., Dancey, C. L., Celik, A. O., Valyrakis, M., Greer, K. and Tanju, A. (2008). The role of impulse on the initiation of particle movement under turbulent flow conditions. *Science* 322(5902), 717–720.

Ferguson, R. (2007). Flow resistance equations for gravel-and boulder-bed streams. *Water Resour. Res.* 43(5), W05427.

Grant, S. B. and Marusic, I. (2011). Crossing turbulent boundaries: Interfacial flux in environmental flows. *Envir. Sci. Tech.* 45, 7107–7113.

Grant, S.B., Azizian, M., Cook, P., Boano, F. and Rippy, M. A. (2018). Factoring stream turbulence into global assessments of nitrogen pollution. *Science* 359(6381), 1266–1269.

Kim, J., Moin, P. and Moser, R. (1987). Turbulence statistics in fully developed channel flow at low Reynolds number. *J. Fluid Mech.* 177, 133–166.

Manes, C., Pokrajac, D., Nikora, V. I., Ridolfi, L. and Poggi, D. (2011). Turbulent friction in flows over permeable walls. *Geophys. Res. Lett.* 38(3), L03402.

Manes, C., Ridolfi, L. and Katul, G. (2012). A phenomenological model to describe turbulent friction in permeable-wall flows. *Geophys. Res. Lett.* 39(14), L14403.

Nelson, J. M., Shreve, R. L., McLean, S. R. and Drake, T. G. (1995). Role of near-bed turbulence structure in bed load transport and bed form mechanics. *Water Resour. Res.* 31(8), 2071–2086.

Nikora, V., McEwan, I., McLean, S., Coleman, S., Pokrajac, D. and Walters, R. (2007). Double-averaging concept for rough-bed open-channel and overland flows: Theoretical background. *J. Hydraul. Eng.* 133(8), 873–883.

Nikora, V., Goring, D., McEwan, I. and Griffiths, G. (2001). Spatially averaged open-channel flow over rough bed. *J. Hydraul. Eng.* 127(2), 123–133.

Nokes R. (2016). Streams. System Theory and Design, University of Canterbury, version 2.05.

O'Connor, B. L. and Hondzo, M. (2008). Dissolved oxygen transfer to sediments by sweep and eject motions in aquatic environments. *Limnol. Oceanogr.* 53(2), 566–578.

Örlü, R. and Schlatter, P. (2011). On the fluctuating wall-shear stress in zero pressure-gradient turbulent boundary layer flows. *Phys. Fluids* 23(2), 21704.

Perot, B. and Moin, P. (1995). Shear-free turbulent boundary layers. Part 1. Physical insights into near-wall turbulence. *J. Fluid Mech.* 295, 199–227.

Robinson, S. K. (1991). Coherent motions in the turbulent boundary layer. *Annu. Rev. Fluid Mech.* 23(1), 601–639.

Roy, A. G., Buffin-Bélanger, T., Lamarre, H. and Kirkbride, A. D. (2004). Size shape and dynamics of large-scale turbulent flow structures in a gravel-bed river. *J. Fluid Mech.* 500, 1–27.

Schmeeckle, M. W. (2014). Numerical simulation of turbulence and sediment transport of medium sand. *J. Geophys. Res-Earth* 119(6), 1240–1262.

Subramanian, C. S., Rajagopalan, S., Antonia, R. A. and Chambers, A. J. (1982). Comparison of conditional sampling and averaging techniques in a turbulent boundary layer. *J. Fluid Mech.* 123, 335–362.

Voermans, J. J., Ghisalberti, M. and Ivey, G. N. (2017). The variation of flow and turbulence across the sediment–water interface. *J. Fluid Mech.* 824, 413–437.

Voermans, J. J., Ghisalberti, M. and Ivey, G. N. (2018). A model for mass transport across the sediment-water interface. *Water Resour. Res.* 54(4), 2799–2812.

Wilson, A. M., Huettel, M. and Klein, S. (2008). Grain size and depositional environment as predictors of permeability in coastal marine sands. *Estuar. Coast Mar. Sci.* 80(1), 193–199.

Figure 1.

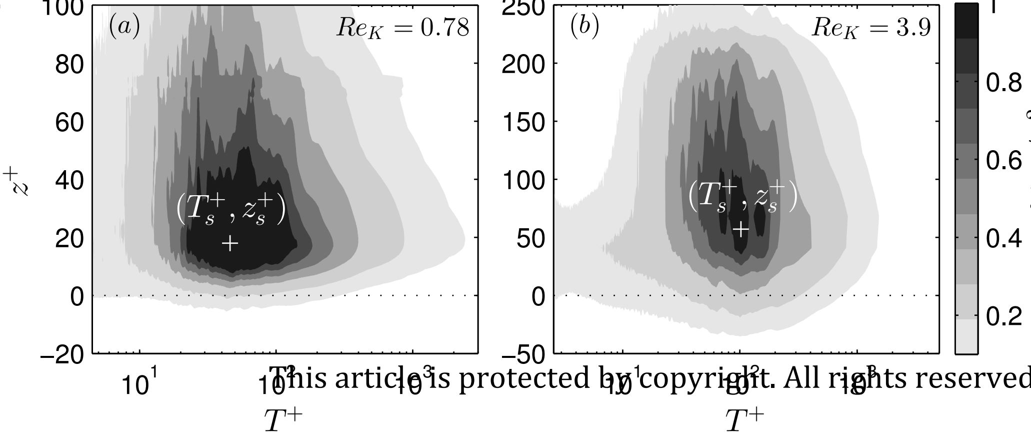
(a)
$Re_K = 0.78$
(T_s^+, z_s^+)
z^+
T^+
(b)
$Re_K = 3.9$
(T_s^+, z_s^+)
T^+
$f\phi_{uu}/u_*^2$

Figure 2.

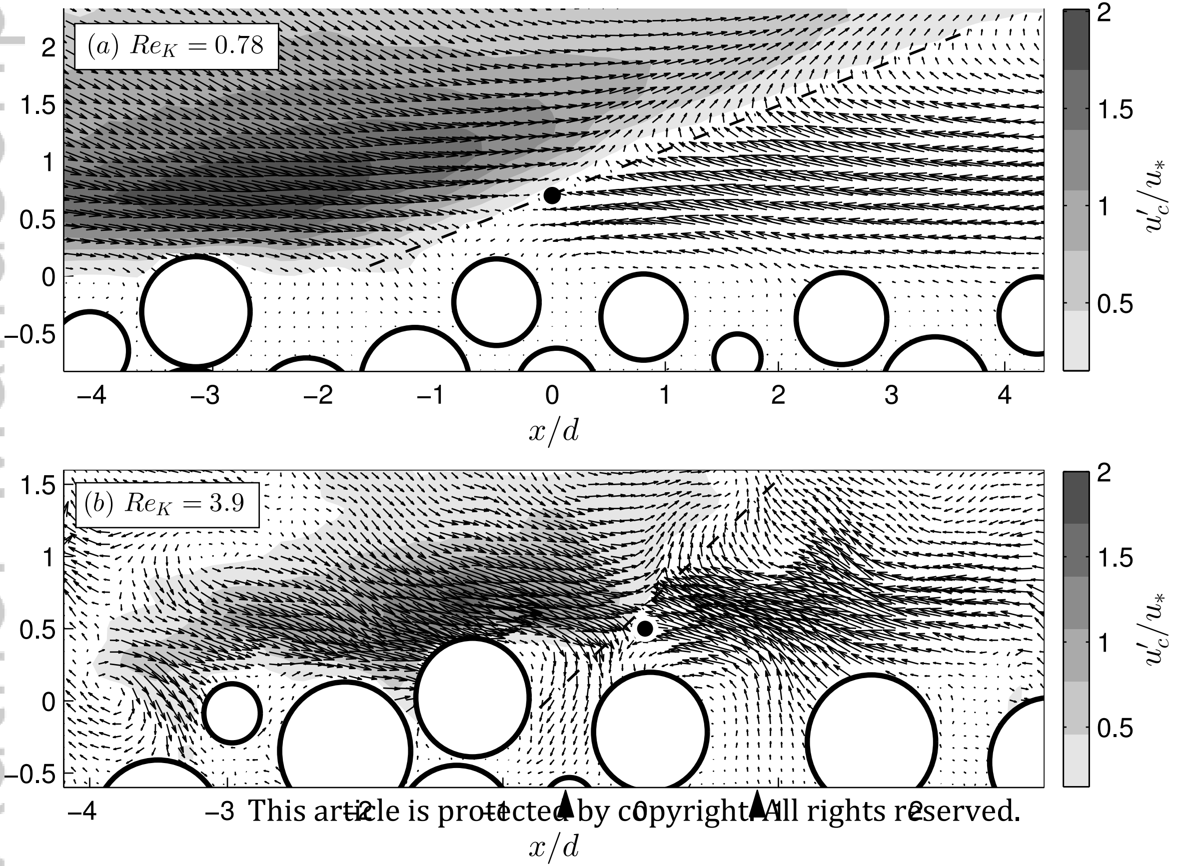
(a) $Re_K = 0.78$
(b) $Re_K = 3.9$
z/d
x/d
u'_c/u_*
2
1.5
1
0.5
0
−0.5
−4
−3
−2
−1
0
1
2
3
4

Figure 3.

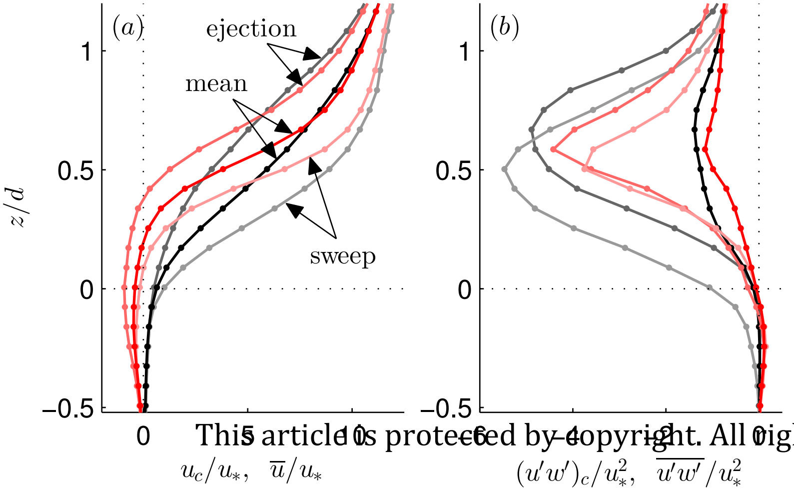
(a)
ejection
mean
sweep
1
0.5
0
−0.5
z/d
0
5
10
u_c/u_*, $\overline{u}/u_*$
(b)
1
0.5
0
−0.5
−6
−4
−2
0
$(u'w')_c/u_*^2$, $\overline{u'w'}/u_*^2$

Figure 4.

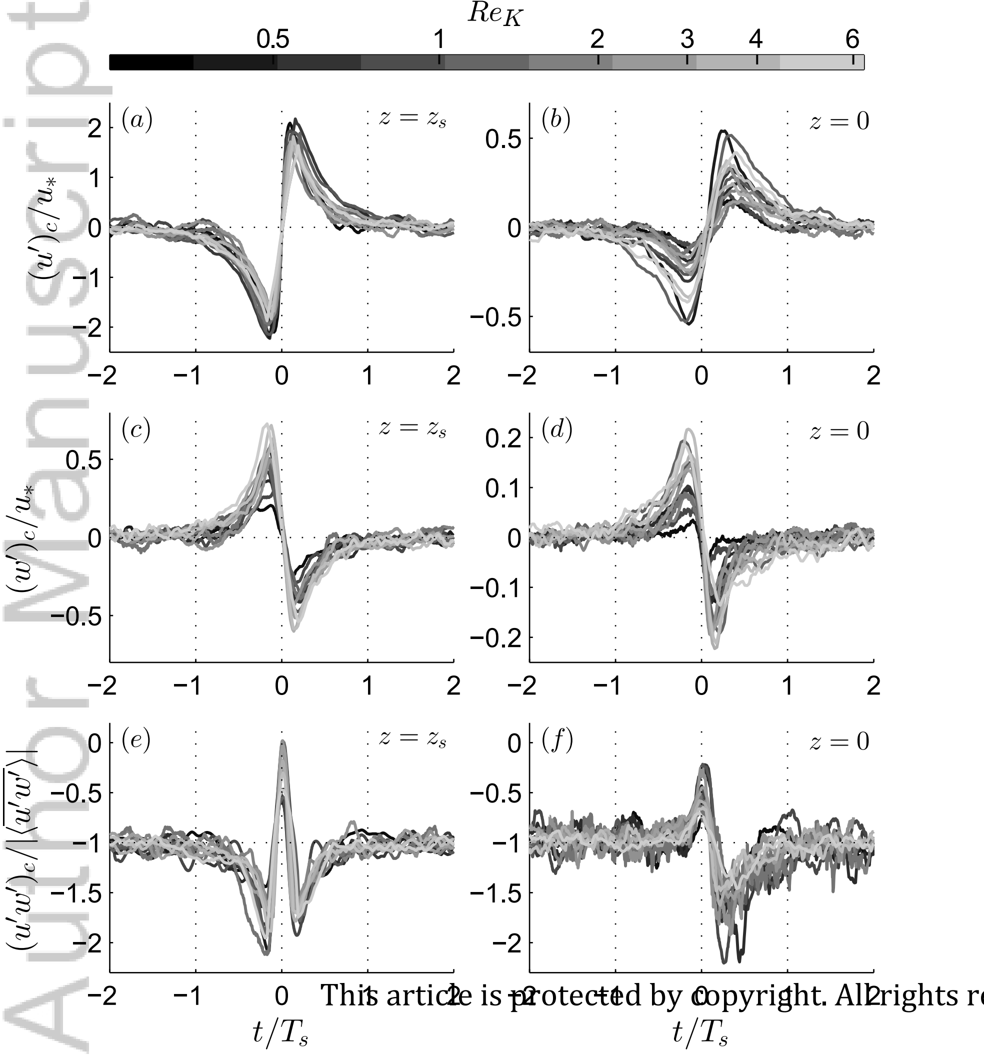
Re_K
0.5
1
2
3
4
6
(a)
$z = z_s$
(b)
$z = 0$
(c)
$z = z_s$
(d)
$z = 0$
(e)
$z = z_s$
(f)
$z = 0$
$(u')_c/u_*$
$(w')_c/u_*$
$(u'w')_c/|\langle\overline{u'w'}\rangle|$
t/T_s
t/T_s

Figure 5.

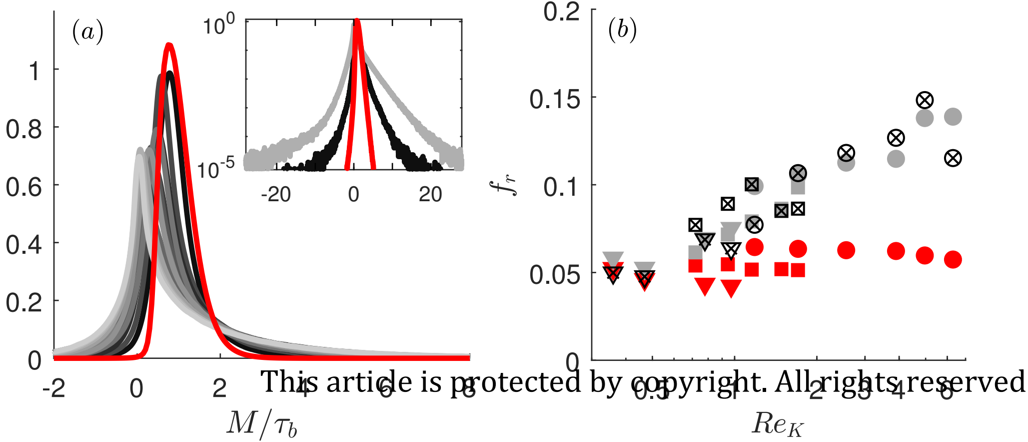

(a)
$P(M/\tau_b)$
M/τ_b
-2
0
2
4
6
8
0
0.2
0.4
0.6
0.8
1
10^0
10^{-5}
-20
0
20
(b)
f_r
Re_K
0
0.05
0.1
0.15
0.2
0.5
1
2
3
4
6

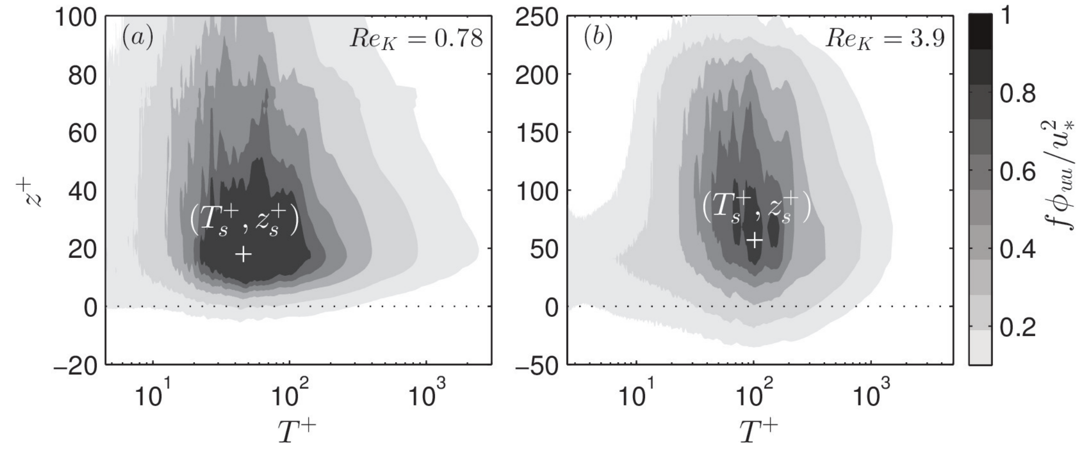

2018gl079850-f01-z-.eps

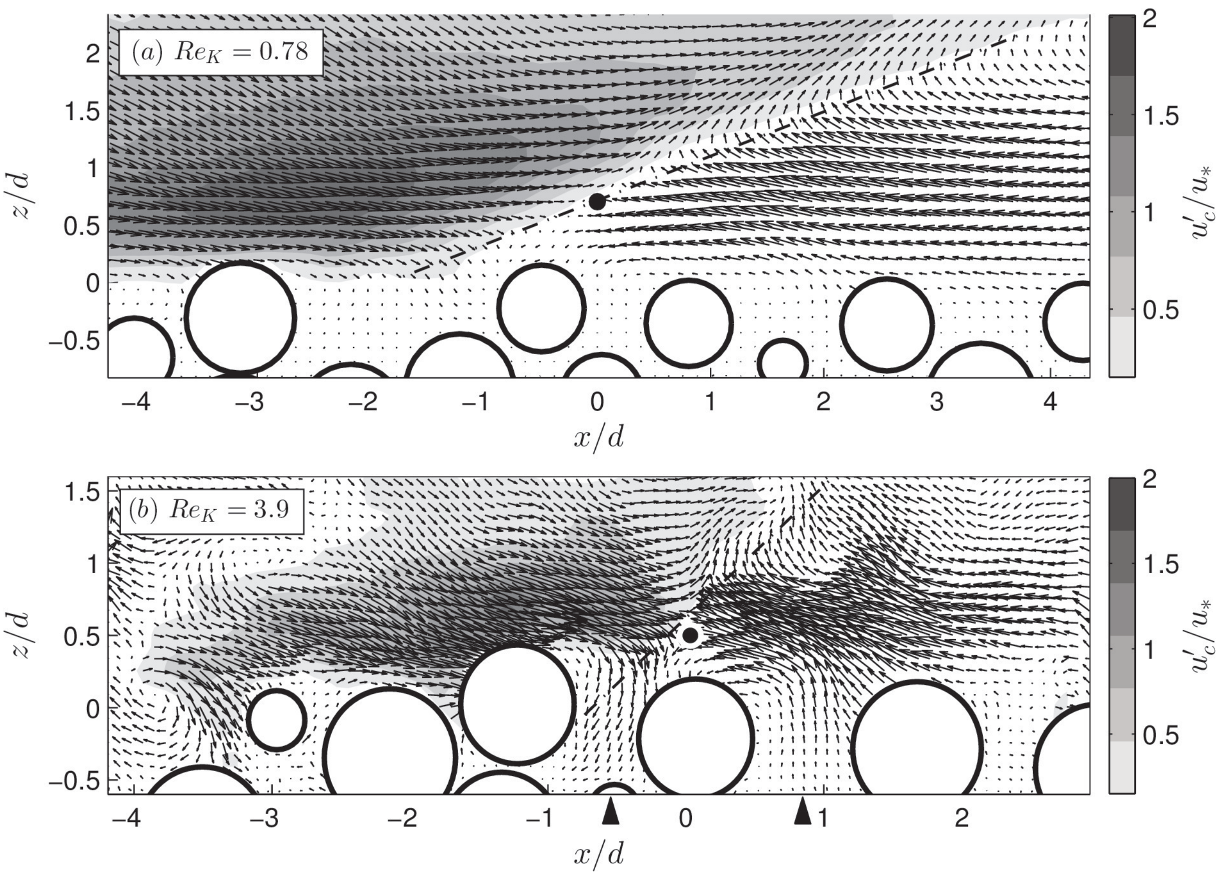

2018gl079850-f02-z-.eps

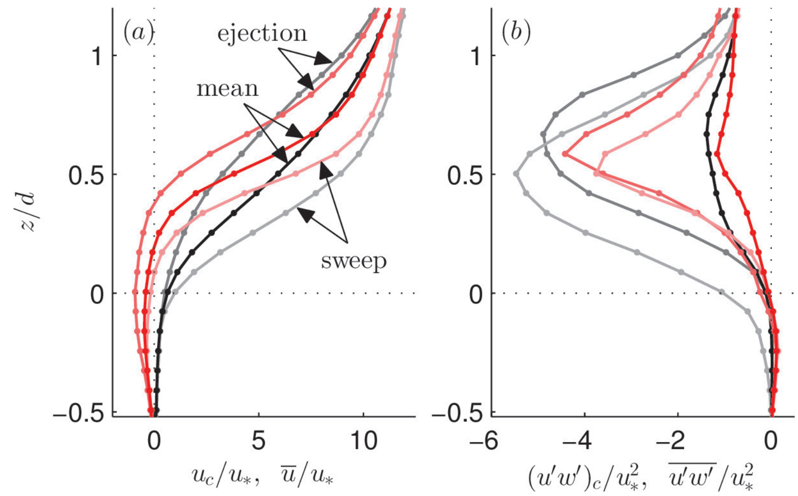

2018gl079850-f03-z-.eps

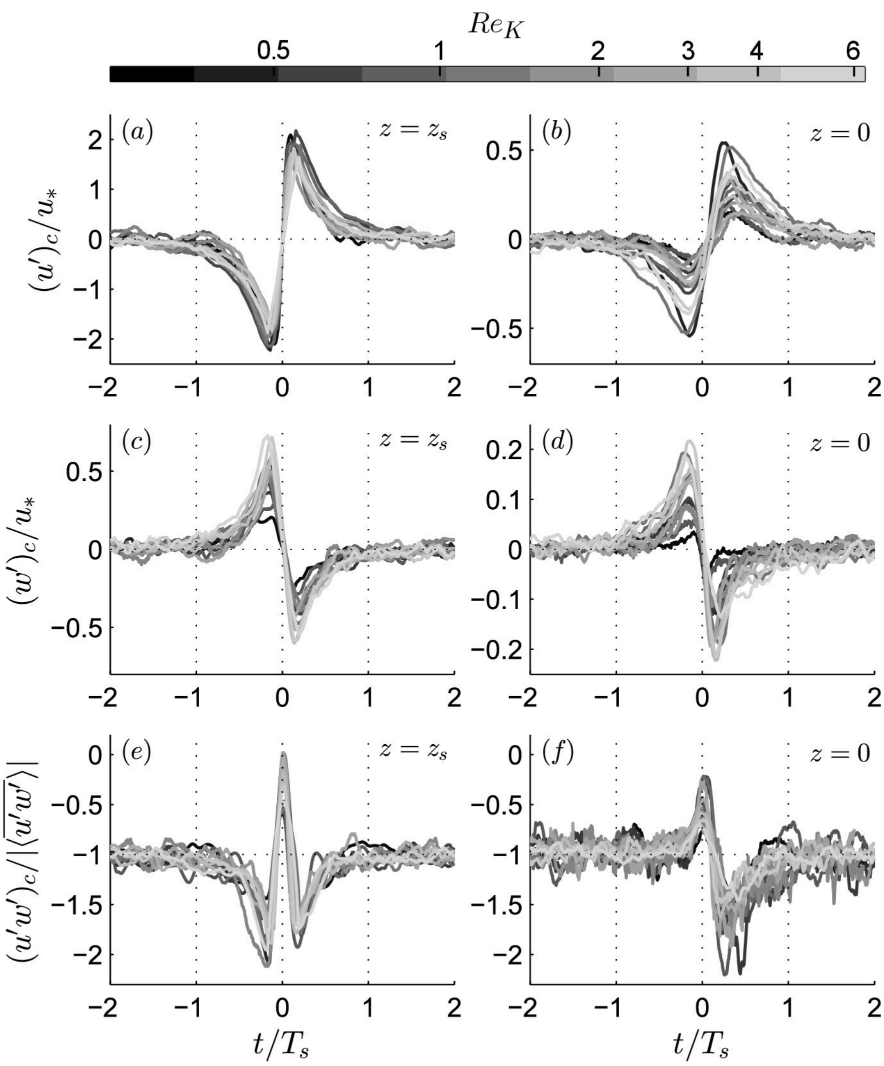

2018gl079850-f04-z-.eps

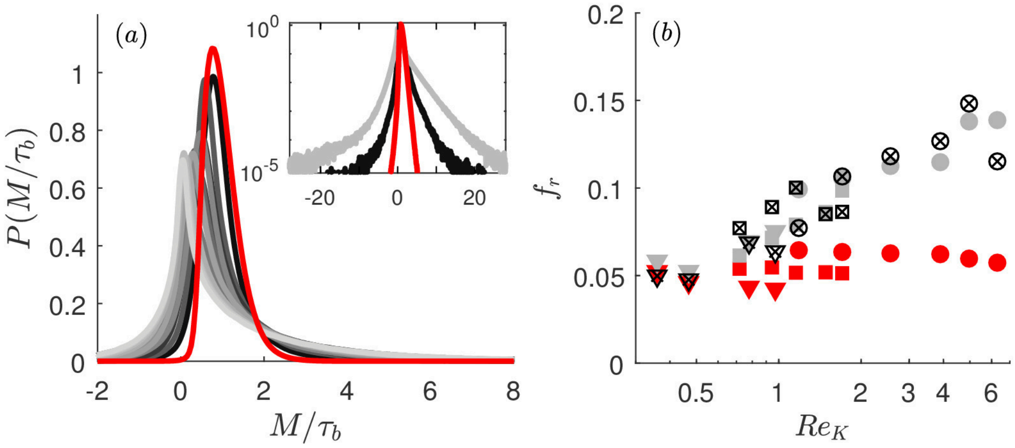

2018gl079850-f05-z-.eps